

Tunable coupler for realizing a controlled-phase gate with dynamically decoupled regime in a superconducting circuit

X. Li,^{1,*} T. Cai,^{1,*} H. Yan,¹ Z. Wang,¹ X. Pan,¹ Y. Ma,¹ W. Cai,¹ J. Han,¹ Z. Hua,¹ X. Han,¹ Y. Wu,¹ H. Zhang,¹ H. Wang,¹ Yipu Song,^{1,†} Luming Duan,^{1,‡} and Luyan Sun^{1,§}

¹Center for Quantum Information, Institute for Interdisciplinary Information Sciences, Tsinghua University, Beijing 100084, China

Controllable interaction between superconducting qubits is desirable for large-scale quantum computation and simulation. Here, based on a theoretical proposal by Yan *et al.* [Phys. Rev. Appl. **10**, 054061 (2018)] we experimentally demonstrate a simply-designed and flux-controlled tunable coupler with a continuous tunability by adjusting the coupler frequency, which can completely turn off adjacent superconducting qubit coupling. Utilizing the tunable interaction between two qubits via the coupler, we implement a different type of controlled-phase (CZ) gate with ‘dynamically decoupled regime’, which allows the qubit-qubit coupling to be only ‘on’ at the usual operating point while dynamically ‘off’ during the tuning process of one qubit frequency into and out of the operating point. This scheme not only efficiently suppresses the leakage out of the computational subspace, but also allows for the acquired two-qubit phase being geometric at the operating point. We achieve an average CZ gate fidelity of $98.3 \pm 0.6\%$, which is dominantly limited by qubit decoherence. The demonstrated tunable coupler provides a desirable tool to suppress adjacent qubit coupling and is suitable for large-scale quantum computation and simulation.

I. INTRODUCTION

As enormous progress has been made towards more complex networks of qubits [1–8], superconducting quantum circuits have become a promising implementation for quantum simulation [9–11] and fault-tolerant quantum computation [12, 13]. Building large circuits requires long coherent times of the qubit, strong interqubit interaction for fast and high-fidelity two-qubit gates, and small to zero coupling between qubits when no interaction is needed. For typical planar circuits with transmon or transmon-type qubits connected through fixed capacitors or quantum buses, strong interaction and variable coupling can be achieved by dynamically adjusting the frequencies of the tunable qubits [4, 14–16] or by applying external microwave drives [17, 18]. Parametric modulation of the frequency of the qubit or the bus has also been used to achieve tunable coupling between qubits [19–29]. However, these approaches could not fully turn off the interaction, and thus parasitic ZZ crosstalk coupling is always present, resulting in a frequency shift of one qubit depending on the state of another. This unwanted qubit interaction could be a limited source to degrade the single-qubit gate performance and to accumulate the entanglement phase error. In addition, because of the requirement of the qubit frequency tunability or the relatively small qubit-qubit detunings, these approaches also suffer from the frequency-crowding problem.

Inserting an extra circuit element, a tunable coupler, can offer another degree of freedom, and thus is efficient for helping mitigate the above problems of unwanted interactions and frequency crowding, while achieving a controllable qubit interaction without introducing other nonidealities that limit the gate performance. A variety of tunable couplers based on a rf superconducting quantum interference device, a tunable bus, or a tunable inductor have previously been designed and demonstrated experimentally [30–42]. Tunable couplers are thus desirable for scalable architectures for quantum compu-

tation and simulation applications.

In this work, following the theoretical proposal in Ref. 43, we experimentally demonstrate a simply designed tunable coupler capacitively coupled to two computational Xmon qubits in a superconducting circuit [12, 44–46]. This tunable coupler is based on only one extra Xmon qubit and is therefore easy to scale up. By adjusting the coupler frequency, the qubit-qubit coupling strength can be tuned through a combination of different coupling paths such that a continuous tunability from positive to negative values can be realized. Consequently, unwanted qubit interactions, such as parasitic ZZ crosstalk, can be completely turned off as wished. Utilizing the tunable interaction between the two qubits via the coupler, we realize the entangling gates of *iswap* and $\sqrt{\text{iswap}}$ with a fidelity of 96.8% and 95.0%, respectively. In addition, we implement a different type of controlled-phase (CZ) gate by using a ‘dynamically decoupled regime’ (DDR) technique, which allows the qubit-qubit coupling to be only ‘on’ at the usual operating point (where the two qubit states $|11\rangle$ and $|20\rangle$ are resonant), while dynamically ‘off’ during the tuning process of one qubit into and out of the operating point by simultaneously tuning the coupler frequency. Compared to the CZ gate implemented with a rectangular pulse or a fast adiabatic pulse [47], this scheme not only efficiently suppresses the leakage out of the computational subspace, but also allows for a geometric π -phase accumulation on $|11\rangle$ state, which is potentially more robust [48]. We achieve an average CZ gate fidelity of $98.3 \pm 0.6\%$, which is dominantly limited by qubit decoherence.

Besides, the demonstrated tunable coupler provides a straightforward way to suppress adjacent qubit coupling without degrading the qubit coherence. Theoretically, this tunable coupler scheme can offer a wide coupling tunability from several MHz in the positive regime to several tens MHz in the negative regime, thus allowing for fast two-qubit gates. The simple design of adding only one extra Xmon qubit as the coupler is also particularly compatible and desirable for large-

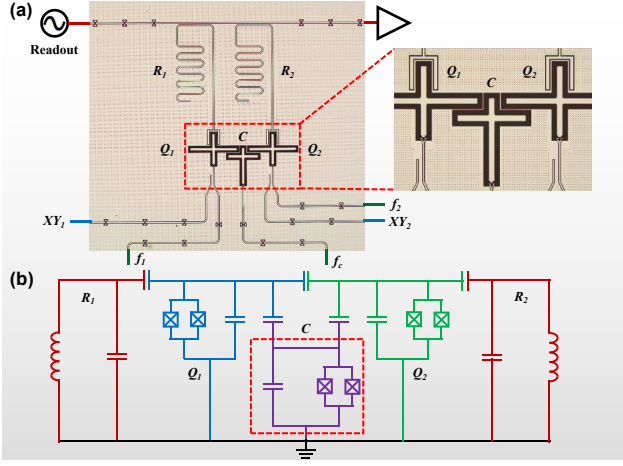


FIG. 1: (a) Optical micrograph of three Xmon qubits with the middle one C serving as a tunable coupler for the two computational qubits (Q_1 and Q_2). Each computational qubit has independent XY and Z control, and is coupled to a separate $\lambda/4$ resonator for simultaneous and individual readout. The coupler also has an individual flux-bias line for a frequency tunability. The combination of direct capacitive coupling and indirect tunable coupling via the coupler constitutes the total coupling between the two computational qubits. (b) Schematic electrical circuit of the device.

scale superconducting architectures.

II. RESULTS

A. Experimental System and Theory

Our experimental device consists of three flux-tunable Xmon qubits (Q_1, C, Q_2) [16, 49, 50] with the middle one C serving as the tunable coupler (henceforth referred to as the ‘coupler’), as shown in Fig. 1(a). Figure 1(b) is the schematic of the device. The maximum frequencies of the two qubits and the coupler are $\omega_1^{\max}/2\pi = 4.961$ GHz, $\omega_2^{\max}/2\pi = 4.926$ GHz, and $\omega_c^{\max}/2\pi = 5.977$ GHz. Details of the experimental apparatus and device parameters are presented in Appendix C. We first briefly discuss the operating principle of the tunable coupler following Ref. 43. The system can be described by the Hamiltonian:

$$H/\hbar = \sum_{i=1,2} \frac{1}{2} \omega_i \sigma_i^z + \frac{1}{2} \omega_c \sigma_c^z + \sum_{i=1,2} g_i (\sigma_i^+ \sigma_c^- + \sigma_c^+ \sigma_i^-) + g_{12} (\sigma_1^+ \sigma_2^- + \sigma_2^+ \sigma_1^-), \quad (1)$$

where ω_α ($\alpha = 1, 2, c$) are the frequencies of Q_1 , Q_2 , and the coupler respectively, $\sigma_\alpha^{z,\pm}$ are the corresponding Pauli Z, raising and lowering operators, g_i ($i = 1, 2$) is the coupling strength between each qubit and the coupler, g_{12} is the direct capacitive coupling strength between the two qubits.

In the strong dispersive regime ($g_i \ll |\Delta_i|$, where $\Delta_i = \omega_i - \omega_c$) and assuming that the coupler mode remains in its ground state, an effective two-qubit Hamiltonian with the variable

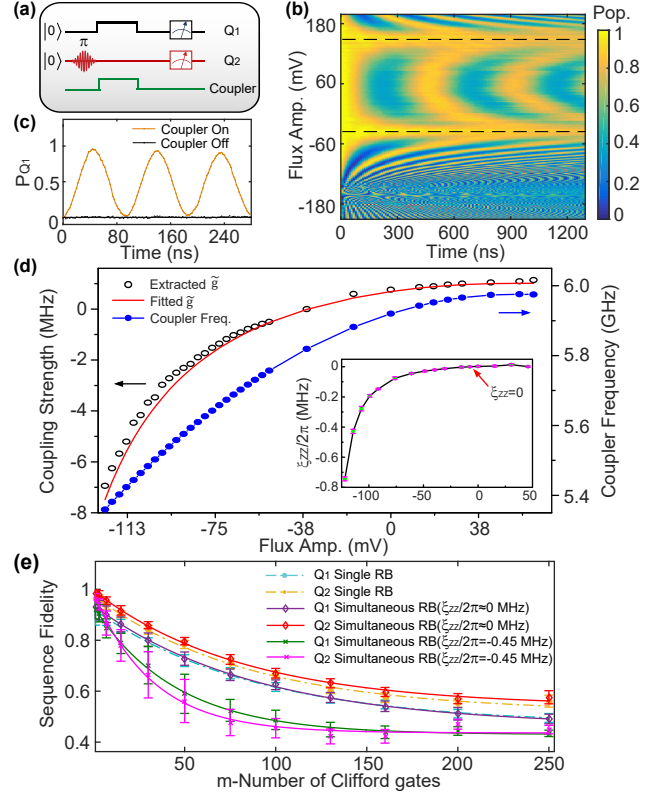


FIG. 2: (a) Pulse sequence to characterize the tunability of the coupler. The two qubits are initialized in the ground state at their sweet spots with a detuning of 35 MHz. The coupler is originally set at $\omega_c/2\pi = 5.905$ GHz where the coupling between the two qubits is nearly off. A π pulse is first to excite Q_2 , followed by two simultaneous fast flux pulses: f_1 brings Q_1 into resonance with Q_2 ; f_c on the coupler to turn on the coupling. After the two qubits interact and evolve for time t , Q_1 and the coupler are pulsed back to the original points for measurements of qubit populations. (b) Population of Q_2 as a function of the amplitude of f_c and t clearly reveals the tunability of the coupling strength. The two dark dashed lines indicate the situation where the coupling is off. (c) Population of Q_1 as a function of time with the coupling on (orange dots) or off (black dots). (d) The effective qubit-qubit coupling strength $\tilde{g}/2\pi$ (black circles) extracted by fitting the oscillation of the qubit excitation in (b) as a function of the flux-bias amplitude on the coupler. The red line is a fit to the extracted \tilde{g} according to Eq. (3). The coupler frequency (blue dots) can be measured independently by probing the dispersive shift of the qubit frequency when pulsing the coupler into the excited state. Inset: the ZZ crosstalk coupling $\xi_{ZZ}/2\pi$ measured in a Ramsey-type experiment when the two qubits are detuned and at their sweet spots. The red arrow indicates where the coupling is off. (e) Individual and simultaneous RB for Q_1 and Q_2 with $\xi_{ZZ}/2\pi \approx 0$ and -0.45 MHz, respectively.

coupler decoupled can be derived by making the unitary transformation $U = \exp\{\sum_{i=1,2} g_i/\Delta_i (\sigma_i^+ \sigma_c^- - \sigma_i^- \sigma_c^+)\}$ [51, 52] and keeping to second order in g_i/Δ_i :

$$UHU^\dagger/\hbar = \sum_{i=1,2} \frac{1}{2} \tilde{\omega}_i \sigma_i^z + \tilde{g} (\sigma_1^+ \sigma_2^- + \sigma_1^- \sigma_2^+), \quad (2)$$

where $\tilde{\omega}_i = \omega_i + g_i^2/\Delta_i$ is the dressed frequency and

$$\tilde{g} = g_{12} + (g_1 g_2)/\Delta \quad (3)$$

is the effective coupling strength with $1/\Delta = (1/\Delta_1 + 1/\Delta_2)/2$. The interaction between the two qubits thus consists of the direct capacitive coupling and the indirect virtual exchange coupling via the coupler. If $\Delta_i < 0$ (the coupler's frequency is above both qubits' frequencies), the virtual exchange interaction term $(g_1 g_2)/\Delta < 0$. Therefore, the effective coupling \tilde{g} can be tuned from negative to positive monotonically with increasing the coupler frequency. Since this coupling tunability is continuous, a critical value ω_c^{off} can always be reached to turn off the qubit-qubit coupling $\tilde{g}(\omega_c^{\text{off}}) = 0$. When the two qubits are detuned, the ZZ crosstalk coupling ξ_{ZZ} can also be turned off (see below and Appendix A).

B. Suppressing Parasitic ZZ Crosstalk

We now demonstrate the tunability of the qubit-qubit coupling strength \tilde{g} controlled by the coupler's frequency. The experimental pulse sequence is illustrated in Fig. 2(a). Coherent excitation oscillation between Q_1 and Q_2 as a function of the flux amplitude of f_c on the coupler and time t is shown in Fig. 2(b), and clearly reveals the change of the coupling strength depending on the coupler frequency. Remarkably, two flux biases of the coupler, at which the qubit-qubit interaction is completely turned off, are observed and marked by two dark dashed lines.

The extracted \tilde{g} indeed varies continuously from positive to negative values and is in good agreement with theoretical calculations (red curve), as shown in Fig. 2(d). The small discrepancy at large negative coupling regime owes to the deviation of the qubit-coupler coupling from the strong dispersive condition. Given the extracted coupling strength and the frequency detuning of each qubit from the coupler, we can estimate the direct capacitive coupling strength $g_{12} \approx 6.74$ MHz using Eq. (3). We note that a large negative interaction can be reached with the decrease of the coupler frequency approaching the qubit frequency. However, when the coupler frequency is further reduced to be close to the qubit frequency, the virtual excitation approximation of the coupler becomes invalid.

We extract ξ_{ZZ} when the two qubits are detuned at their sweet spots using a Ramsey-type experiment, which involves probing the frequency of Q_2 with Q_1 in either its ground or excited state [53, 54]. The measured ξ_{ZZ} also depends on the coupler frequency and is shown in the inset of Fig. 2(d). At the critical coupler frequency $\omega_c^{\text{off}} \approx 5.905$ GHz, indicated by the red arrow, the measured $\xi_{ZZ}/2\pi \approx 1$ kHz and is limited by the current detection scheme. We utilize simultaneous randomized benchmarking (RB) to verify the isolation of two qubits at this configuration. The simultaneous RB gate fidelities of 99.45% and 99.40% are nearly the same as the individual RB gate fidelities of 99.44% and 99.41% for Q_1 and Q_2 respectively, as shown in Fig. 2(e). For comparison, when the two qubits are biased in the same configuration as above but with

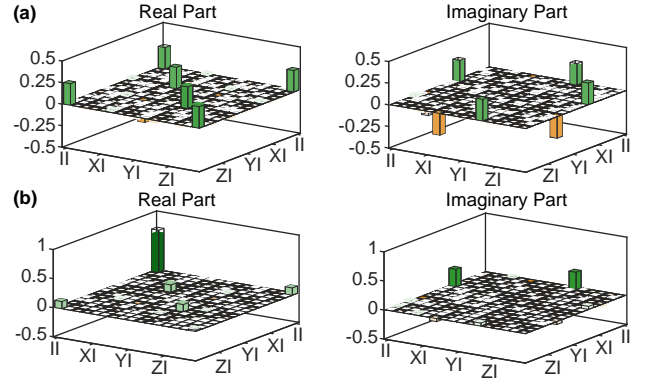


FIG. 3: (a) (b) Bar charts of the measured χ_{exp} from a QPT for iswap and $\sqrt{\text{iswap}}$ with a gate fidelity of 96.8% and 95.0%, respectively. The solid black outlines are for the ideal gate.

$\xi_{ZZ}/2\pi = -0.45$ MHz, the simultaneous RB gate fidelities on both qubits are lowered by about 0.54% (Q_1) and 0.93% (Q_2). This contrast illustrates the importance of the tunable coupler for precise qubit control.

C. Implementing CZ Gate with Dynamically Decoupled Regime

With the tunability of the coupling, we now move to the implementation of two-qubit entangling gates. The iswap and $\sqrt{\text{iswap}}$ gates are quite natural based on the Hamiltonian of Eq. (2) [37]. Their measured χ_{exp} from quantum-process tomography (QPT), which can give full information about the gate process [55], are presented in Fig. 3 with a gate fidelity of 96.8% and 95.0% respectively. Here we focus on the controlled-phase (CZ) gate. The CZ gate is implemented by using the usual avoided crossing of the noncomputational state $|20\rangle$ with the $|11\rangle$ state [Fig. 4(a)], which is only accessible to $|11\rangle$ and thus provides the conditional nature of the gate to flip the phase if and only if both qubits are excited [15, 56–58].

The fully controllable interaction of the coupler allows for turning the coupler ‘on’ or ‘off’ as wished. The ideal scheme of implementing a CZ gate with a coupler is to have both qubits initialized in the operating point where $|11\rangle$ and $|20\rangle$ have the same energy with the coupling ‘off’, and then slowly turn on the coupler for proper time to implement the gate. This method can avoid adjusting the qubit frequency, and thus reduce the leakage error. However, the unwanted crosstalk of the XY control lines in our device could degrade single-qubit gate performance because of the zero detuning between ω_{12} of Q_1 and ω_{01} of Q_2 . Therefore, the qubits are initially detuned and at their sweet spots with the coupling ‘off’.

The simplest case is to use rectangular fluxes to simultaneously pulse the qubits to the avoided-crossing point and turn on the coupling. Both our measurement and simulation reveal that the leakage out of $|11\rangle$ can be effectively suppressed in the positive coupling regime rather than the negative one. This is evidenced by the observation of high-frequency oscil-

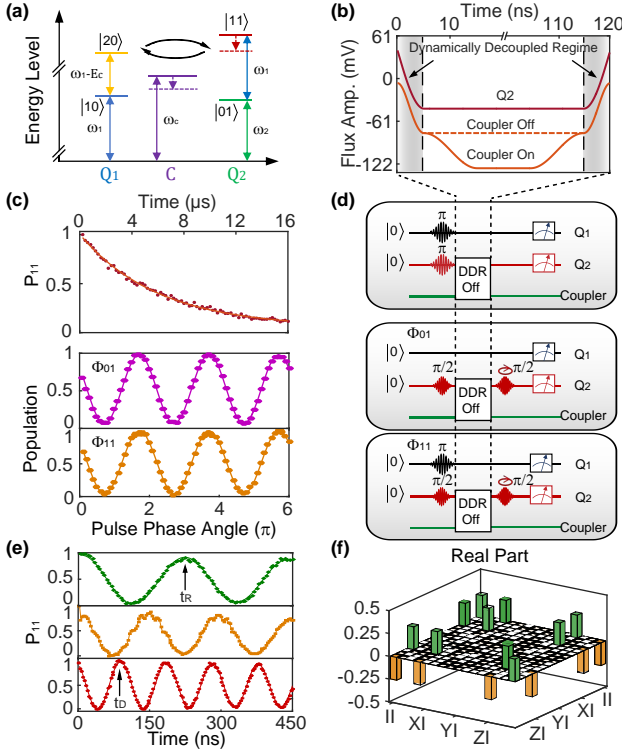


FIG. 4: (a) Schematic to realize the CZ gate using the usual $|11\rangle$ and $|20\rangle$ resonance. (b) Flux sequence to realize the CZ gate with DDR. The Q_1 frequency is unchanged during the process. A gradual flux pulse (for a cosine-type frequency adjustment) on Q_2 is to tune its frequency to the operating point, while a flux pulse on the coupler with an appropriate pulse shape to dynamically keep the coupling ‘off’ (the shaded regions). The coupling is then turned on by applying another gradual flux pulse on the coupler (for a cosine-type coupler frequency adjustment) for proper two-qubit interaction time to acquire the required π -phase shift on $|11\rangle$. (c), (d) Confirmation of the ‘off’ state of the coupling in the DDR and the corresponding measurement sequences. Top: the population of $|11\rangle$ state shows purely exponential decay without any oscillation. Middle: phase accumulation of $|01\rangle$ with respect to $|00\rangle$. Bottom: phase accumulation of $|11\rangle$ with respect to $|10\rangle$. The difference between the lower two panels shows zero phase accumulation of $|11\rangle$, confirming zero coupling. (e) Population of $|11\rangle$ in three different schemes to realize the CZ gate. Upper: rectangular pulses to have a positive coupling strength. $t_R = 222$ ns is required for realizing the standard two-qubit CZ gate. Middle: rectangular pulses to have a negative coupling regime. Obvious high-frequency oscillations occur and indicate the leakage out of $|11\rangle$. Lower: DDR pulses to have a large negative coupling but with a smooth oscillation. A CZ gate can be accomplished with a gate time $t_D = 119$ ns. (f) Bar chart of the measured real part of χ_{exp} from a QPT shows a gate fidelity of $98.3 \pm 0.6\%$. The solid black outlines are for the ideal gate.

lations [the middle panel in Fig. 4(e)], which cause unwanted leakage error. However, due to the weak positive coupling strength, a relatively long gate time ($t_R = 222$ ns) is required to accomplish the CZ gate. The average CZ gate fidelity is 95.5% from the QPT measurement.

To improve the gate fidelity, we use a ‘dynamically decoupled regime’ (DDR) scheme to implement the CZ gate. Note

that DDR defined here differs in explication from the term ‘dynamical decoupling’ used in coherent control pulse methods to suppress the dephasing error [59]. This scheme can not only efficiently suppress the leakage out of the computational subspace but also allow us to perform the gate in the negative coupling regime with larger interaction strength for a shorter gate time. The DDR scheme can be understood by mapping the interaction between the states $|11\rangle$ and $|20\rangle$ onto a Hamiltonian of a qubit $H = H_x \sigma'_x + H_z \sigma'_z$ [47], where H_x is the coupling energy between the states $|11\rangle$ and $|20\rangle$, H_z is the frequency detuning of $|11\rangle$ from the resonance point of the avoided crossing, and σ'_x and σ'_z are the corresponding Pauli operators which are distinguished from those on the computational qubit. For the typical direct coupling scheme without a coupler where the coupling energy σ'_x term is fixed, CZ gate is realized by adjusting only the σ'_z term, such as the one implemented with a rectangular pulse, fast adiabatic pulse or nonadiabatic pulse [47, 58]. While for the DDR scheme with a coupler, both σ'_x term and σ'_z term can be varied as wished.

The experimental flux sequence is shown in Fig. 4(b). We use a gradual flux pulse on Q_2 to tune its frequency to the operating point, while dynamically keeping the coupling ‘off’. This DDR is achieved by applying a flux pulse on the coupler with an appropriate pulse shape calculated by Eq. (3) and is further optimized to assure the zero coupling during the whole qubit frequency-changing process [the shaded regions where $H_x = 0, H_z = H_z(t)$]. After that, we slowly turn on the coupling by applying another gradual flux pulse on the coupler and wait for proper time for the two-qubit interaction to acquire the π -phase shift on $|11\rangle$ [$H_x = H_x(t), H_z = 0$]. The ‘off’ state of the coupling in the DDR is confirmed by measuring the population change and phase accumulation of $|11\rangle$ state with the same flux pulses as in Fig. 4(b) (the DDR and the dashed line in the middle). The experimental results and sequences are shown in Figs. 4(c) and 4(d), respectively.

We choose an appropriate negative coupling strength to perform the CZ gate, balancing the gate time and qubit-coupler leakage induced by the non-negligible excitation of the coupler. The larger interaction strength reduces the CZ gate time to $t_D = 119$ ns [bottom panel in Fig. 4(e)] and the gate fidelity is improved with an average QPT fidelity of $98.3 \pm 0.6\%$. The measured χ_{exp} is shown in Fig. 4(f). Moreover, the observed two-qubit π -phase accumulation is geometric, which is potentially noise resilient to frequency fluctuation during the gate operation. The coupler frequency can be further lowered for a higher coupling strength such that the CZ gate time can be reduced to $t_D = 68$ ns. However, due to a larger leakage between the qubit and the coupler, the gate fidelity is slightly lower. It is worth mentioning that we also consider a synchronization optimization strategy to mitigate leakages from not only the qubit-qubit $|01\rangle$ and $|10\rangle$ swap channel but also the qubit-coupler real-energy exchange channel [60].

III. DISCUSSION

Because the tunable coupler provides an extra degree of freedom and can fully suppress the qubit coupling, the CZ gate with the DDR scheme should be insensitive to qubit parameters. Based on a numerical simulation (see Appendix E), in the absence of qubit decoherence, the QPT fidelity of the CZ gate with the DDR scheme can be above 99.99% (with ‘mesolve’ in QuTip [61, 62]). For comparison, we also numerically simulate the CZ gate implemented for the direct coupling case with a fast adiabatic pulse [47]. We choose the same qubit idle frequencies and qubit-qubit coupling strength to ensure the same gate time (~ 120 ns) as the DDR scheme, and include the first three coefficients of Fourier basis functions in the pulse optimization with the ‘fmin’ function in PYTHON. The resulted maximum CZ gate fidelity $F \approx 99.60\%$, with an error significantly larger than that from the DDR scheme, because the fast adiabatic pulse is more sensitive to qubit parameters and pulse optimization. We note that more Fourier coefficients in the fast adiabatic pulse can be included to improve the CZ gate fidelity, but at the expense of more optimization parameters and harder optimization. A high-fidelity, fast adiabatic CZ gate would be even more challenging because of the unwanted crosstalk when the qubit system becomes larger. By contrast, the CZ gate with the DDR scheme should maintain its robustness and convenience, and therefore would be particularly suitable for large-scale superconducting circuits.

In current experiment, the measured CZ gate fidelity is dominantly limited by the qubit decoherence, while the coupler decoherence has little effect on the gate fidelity since the coupler remains in the ground state. Optimization of coupler design for better parameters would be helpful to achieve a higher coupling strength while decreasing the leakage error and consequently get a shorter CZ gate time with a improved gate performance. Besides, other pulse shapes to turn on the coupling may further suppress the leakage and need future exploration. In addition, improving fabrication technology to minimize crosstalk between XY lines can offer possibility of realizing a more ideal CZ gate [63]. Finally, by adopting the Nelder-Mead optimization protocol [64], we could further improve the CZ gate fidelity to a higher level.

In summary, we experimentally realize a simple prototype of a flux-controlled tunable coupler. The competition between the positive direct and negative indirect coupling allows for a continuous tunability and for switching off the coupling completely. With this coupler, we implement two-qubit entangling iswap, $\sqrt{\text{iswap}}$, and CZ gates. In particular, the CZ gate is realized with fully dynamical control over the qubit-qubit coupling: the coupling is only on at the operating point to acquire a geometric two-qubit phase, while being off during the tuning process of the qubit frequency. We achieve an average CZ gate fidelity of $98.3 \pm 0.6\%$, characterized via QPT and dominantly limited by system decoherence. The demonstrated tunable coupler therefore provides a desirable tool to suppress adjacent qubit coupling and is suitable for large-scale quan-

tum computation and simulation [9–11, 65].

Acknowledgments

We thank Chengyao Li for the technical support, and Changling Zou and Zhengyuan Xue for valuable discussions. This work is supported by National Key Research and Development Program of China under Grant No. 2016YFA0301902 and 2017YFA0304303, and National Natural Science Foundation of China under Grant No.11874235 and No.11925404.

Appendix A: Calculation of the effective qubit coupling \tilde{g} and ZZ crosstalk coupling ξ_{ZZ}

To study the tunable coupling strength between Q_1 and Q_2 , we consider the system Hamiltonian,

$$\begin{aligned}\hat{H} &= \hat{H}_0 + \hat{V} \\ \hat{H}_0/\hbar &= \sum_{i=1,2,c} \omega_i a_i^\dagger a_i + \frac{\eta_i}{2} a_i^\dagger a_i^\dagger a_i a_i \\ \hat{V}/\hbar &= \sum_{j=1,2} g_{jc} (a_j^\dagger a_c + a_j a_c^\dagger) + g_{12} (a_1^\dagger a_2 + a_1 a_2^\dagger)\end{aligned}\quad (\text{A1})$$

where ω_i and η_i ($i = 1, 2, c$) are the frequencies and anharmonicities of Q_1 , Q_2 , and the coupler respectively, a_i^\dagger and a_i are the corresponding raising and lowering operators, g_{jc} ($j = 1, 2$) is the coupling strength between each qubit and the coupler, and g_{12} is the direct capacitive coupling strength between the two qubits.

When we only consider the ground and the first excited states of the Xmon qubits, based on the Schrieffer-Wolff transformation [51, 52], the effective coupling \tilde{g} between Q_1 and Q_2 would be [43],

$$\tilde{g} = \frac{g_{2c}g_{1c}}{2\Delta_{2c}} + \frac{g_{2c}g_{1c}}{2\Delta_{1c}} + g_{12}, \quad (\text{A2})$$

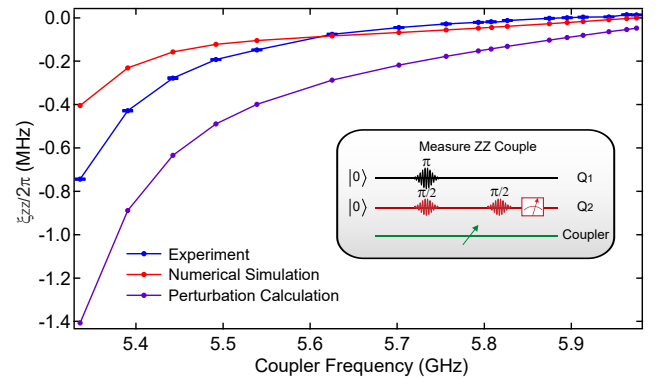


FIG. 5: ZZ crosstalk coupling ξ_{ZZ} versus coupler frequency when the two qubits are detuned and at their sweet spots as in the inset of Fig. 2 of the main text. Inset: the experimental sequence for measuring ZZ crosstalk coupling ξ_{ZZ} at a specific coupler flux bias.

where $\Delta_{ic} \equiv \omega_i - \omega_c$ is the frequency detuning between the qubit and the coupler.

To calculate the parasitic ZZ crosstalk coupling ξ_{ZZ} between Q_1 and Q_2 when they are detuned, however, it is not enough to only keep up to the second order in the Schrieffer-Wolff transformation. Here we use the perturbation approach [66, 67] to derive the parasitic ZZ crosstalk coupling to second, third, and fourth order of the Hamiltonian (A1). We define $\xi_{ZZ} = \omega_{11} - \omega_{01} - \omega_{10}$ between Q_1 and Q_2 . The corresponding perturbation terms are:

$$\xi_{ZZ}^{(2)} = \frac{2(g_{12})^2(\eta_1 + \eta_2)}{(\Delta_{12} + \eta_1)(\Delta_{12} - \eta_2)}, \quad (\text{A3})$$

$$\begin{aligned} \xi_{ZZ}^{(3)} = & 2g_{12}g_{1c}g_{2c} \left[\frac{1}{\Delta_{2c}} \left(\frac{2}{\Delta_{21} - \eta_1} - \frac{1}{\Delta_{21}} \right) \right. \\ & \left. + \frac{1}{\Delta_{1c}} \left(\frac{2}{\Delta_{12} - \eta_2} - \frac{1}{\Delta_{12}} \right) \right], \end{aligned} \quad (\text{A4})$$

$$\begin{aligned} \xi_{ZZ}^{(4)} = & \frac{2(g_{1c})^2(g_{2c})^2}{\Delta_{1c} + \Delta_{2c} - \eta_c} \left(\frac{1}{\Delta_{1c}} + \frac{1}{\Delta_{2c}} \right)^2 \\ & + \frac{(g_{1c})^2(g_{2c})^2}{(\Delta_{1c})^2} \left(\frac{2}{\Delta_{12} - \eta_2} - \frac{1}{\Delta_{12}} - \frac{1}{\Delta_{2c}} \right) \\ & + \frac{(g_{1c})^2(g_{2c})^2}{(\Delta_{2c})^2} \left(\frac{2}{\Delta_{21} - \eta_1} - \frac{1}{\Delta_{21}} - \frac{1}{\Delta_{1c}} \right), \end{aligned} \quad (\text{A5})$$

where $\Delta_{ij} \equiv \omega_i - \omega_j$ ($i, j = 1, 2, c; i \neq j$). Because $g_{12} \ll g_{ic}$, we omit the g_{12} term in the derivation of the fourth-order perturbation. Finally, $\xi_{ZZ} = \xi_{ZZ}^{(2)} + \xi_{ZZ}^{(3)} + \xi_{ZZ}^{(4)}$ and the perturbation calculation is compared with the experiment and the numerical simulation based on QuTip [61, 62], as shown in Fig. 5. The experiment agrees fairly well with the numerical simulation. The deviation between the experiment and the perturbation calculation may be due to the higher-order terms. When the detuning between the coupler and the qubits decreases, we can see a larger deviation, indicating the higher-order perturbation terms become more important. The experiment, simulation, and perturbation calculation all reveal that ξ_{ZZ} can be tuned from negative to positive continuously, and thus we can always find a critical point to fully turn off ξ_{ZZ} between Q_1 and Q_2 .

Appendix B: Quantum Process Tomography

The two-qubit quantum gates are characterized with quantum-process tomography (QPT). Generally, the qubits are initialized to the following 16 states $\{|g\rangle, |e\rangle, (|g\rangle + |e\rangle)/\sqrt{2}, (|g\rangle - i|e\rangle)/\sqrt{2}\}^{\otimes 2}$ with the proper single-qubit rotations. After the gate that needs to be characterized, the corresponding final two-qubit state is reconstructed from state tomography measurements with 16 prerotations $\{I, X/2, Y/2, X\}^{\otimes 2}$, where I is the identity operator, $X, Y, X/2$, and $Y/2$ are single-qubit π and $\pi/2$ rotations around X and Y

axes respectively. With the 16 initial states ρ_i , the experimental process matrix χ_{exp} can be extracted from the 16 corresponding final states ρ_f through $\rho_f = \sum_{m,n} \chi_{mn} E_m \rho_i E_n^\dagger$ [68], where the basis operators E_m and E_n are chosen from the set $\{I, \sigma_x, -i\sigma_y, \sigma_z\}^{\otimes 2}$.

However, the real experiment is not perfect. For example, the generated ρ_i are not ideal due to the initial state preparation errors; the final state tomography could also be nonideal due to the readout errors. To solve this problem, we first use state tomography to characterize the preparation of the initial states. The measured initial states ρ_i^{meas} are then used to extract χ_{exp} through $\rho_f = \sum_{m,n} \chi_{mn} E_m \rho_i^{\text{meas}} E_n^\dagger$. The gate-process fidelity is finally calculated through $F = \text{Tr}(\chi_{\text{exp}} \chi_{\text{ideal}})$, where χ_{ideal} is the ideal process matrix for the corresponding gate.

Appendix C: Device Fabrication, Experimental Setup, and Device Parameters

Our experimental device consists of three flux-tunable Xmon qubits (Q_1, C, Q_2) with the middle one C serving as the tunable coupler. Fabrication of this sample includes three main steps: (1) aluminum deposition onto a c -plane sapphire substrate followed by photolithography and inductively coupled-plasma etching to define all the base wiring and resonators; (2) two photolithography processes, aluminum deposition, and wet etching to construct airbridges [69]; (3) e-beam lithography with two layer e-beam resists and double-angle aluminum deposition to make Josephson junctions. Airbridges are mainly used to connect segments of ground planes in order to reduce parasitic slotline modes. We also apply flux trapping holes (square holes of side length of $2 \mu\text{m}$) to reduce magnetic vortices loss [70].

The full parameters of the qubits and the coupler are shown in Table I with the coupling capacitances defined in Fig. 6. Our sample is measured in a dilution refrigerator with a base temperature about 20 mK, and the details of our measurement circuit are shown in Fig. 7. We use two XY control lines to manipulate the qubit states, three flux lines to modify the qubit and the coupler frequencies, and one input-output line to readout both qubits simultaneously. The XY control pulses are generated from a signal generator modulated by a four-channel arbitrary waveform generator (AWG), while flux pulses are directly generated from AWGs. Finally, a broad-

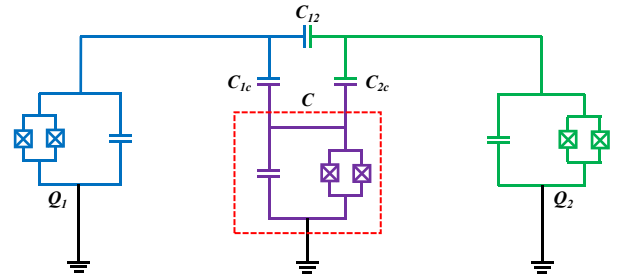


FIG. 6: Schematic electrical circuit of the device.

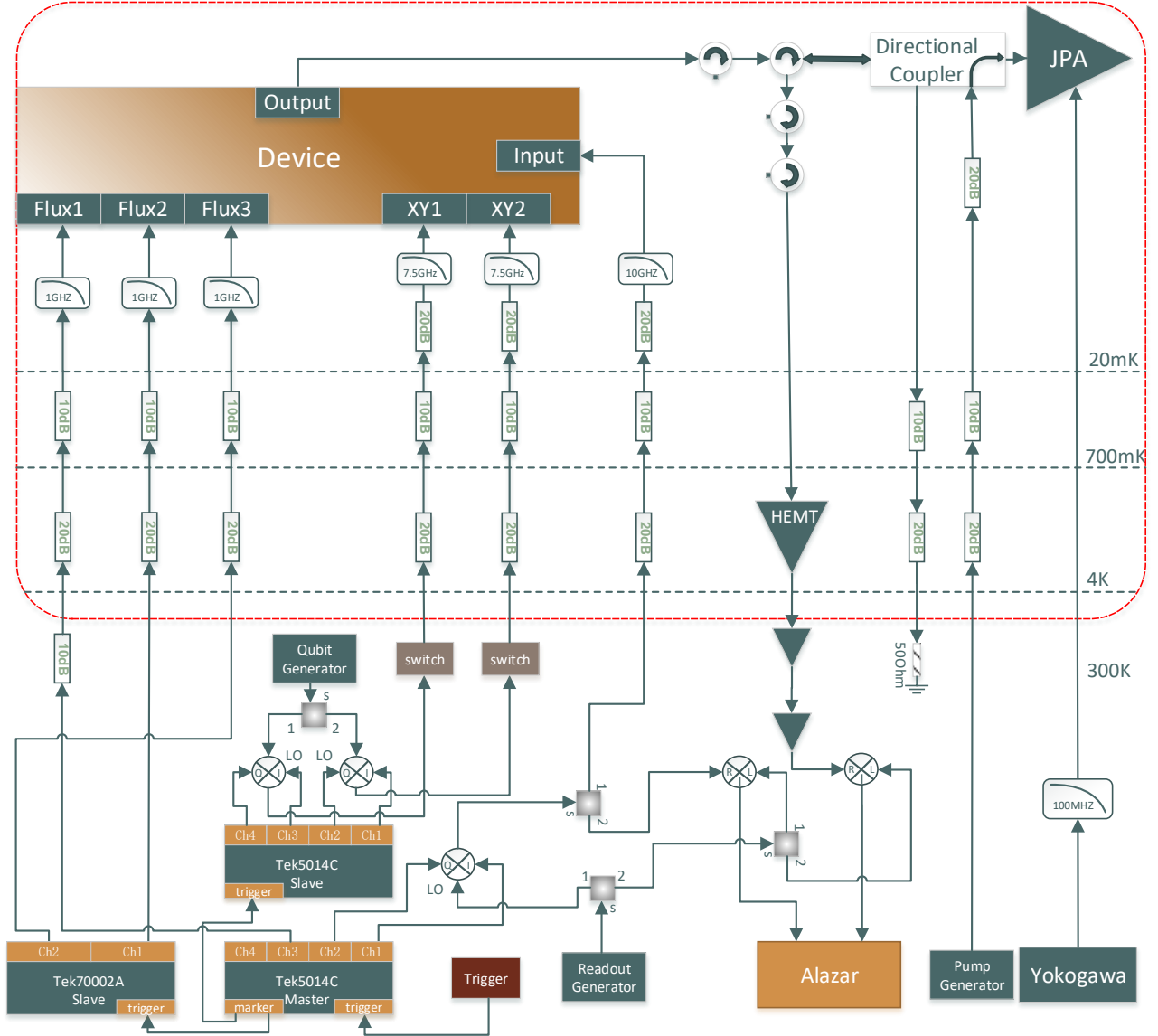


FIG. 7: Measurement setup. Our measurement circuit contains three AWGs (two Tek5014C and one Tek70002A), three signal generators, and other microwave components. The XY control pulses are generated from a signal generator modulated by the AWG. Flux pulses are generated directly from Tek5014C (for Q_1) and Tek70002A (for Q_2 and the coupler). Readout signal is amplified by a JPA at the base, a high-electron-mobility-transistor (HEMT) amplifier at 4K and two room-temperature amplifiers, and finally down-converted and digitized by an analog-to-digital converter (ADC).

band Josephson parametric amplifier (JPA) [71–74] is used for high-fidelity simultaneous single-shot readout.

Derivative removal adiabatic gate (DRAG) [75] pulse is used for single qubit rotation to reduce the leakage to higher qubit levels. Due to thermal population of the qubits and the coupler, and nonperfect separation of the ground and excited states for each qubit, the qubit readout results are reconstructed by using Bayes' rule with a calibration matrix:

$$M_{Bj} = \begin{pmatrix} F_{gj} & 1 - F_{ej} \\ 1 - F_{gj} & F_{ej} \end{pmatrix},$$

where F_{gj} and F_{ej} are the readout fidelity for the j -th ($j = 1, 2$) qubit in the initial steady state without and with a following π rotation respectively. The calibration process is similar to that in Ref. 26.

Besides, we measure the flux-line-crosstalk matrix M_z among the flux control lines (both qubits and the coupler) in the device. Although there is no readout cavity for the coupler, the coupler frequency can still be measured through the qubit-coupler dispersive shift (discussed below). The inverse of M_z gives the orthogonalization matrix \tilde{M}_z which allows for

independent control of the only desired qubit or the coupler:

$$\tilde{M}_z = M_z^{-1} = \begin{pmatrix} 0.9963 & 0.0096 & 0.0264 \\ -0.0798 & 0.9997 & 0.0094 \\ -0.0116 & 0.0384 & 0.9974 \end{pmatrix}$$

The small flux-line-crosstalk is due to the good ground-plane connection by using airbridges even though the coupler is geometrically close to the two qubits.

TABLE I: Device parameters.

| Qubit parameter | Q_1 | Q_2 |
|-----------------------------------|------------|------------|
| Readout resonator frequency (GHz) | 6.825 | 6.864 |
| Qubit maximum frequency (GHz) | 4.961 | 4.926 |
| T_1 (sweet point) (μ s) | 14 | 13.7 |
| T_2 (sweet point) (μ s) | 8.4 | 4 |
| T_{2E} (sweet point) (μ s) | 8.7 | 4.4 |
| $\eta/2\pi$ (MHz) | -206 | -202 |
| $\chi_{qr}/2\pi$ (MHz) | -0.4 | -0.4 |
| $g_{qr}/2\pi$ (MHz) | 86.6 | 90.6 |
| Coupler parameter | Simulation | Experiment |
| $\eta_c/2\pi$ (MHz) | -254 | |
| $C_{ic}(i=1,2)$ (fF) | 2.4 | |
| C_{12} (fF) | 0.13 | |
| Coupler frequency (GHz) | 6.3 | 5.977 |
| $g_{ic}/2\pi$ ($i=1,2$) (MHz) | 81.3 | 76.9 |
| $g_{12}/2\pi$ (MHz) | 3.8 | 6.74 |

Appendix D: More Measurement Results

1. Coupler spectrum and qubit-coupler coupling strength

In our experiments, due to the lack of the readout resonator for the coupler, we cannot directly detect the coupler's thermal population and spectrum. Here, we just simply assume a similar thermal population for both the coupler and the computational qubits. We can, however, indirectly probe the coupler spectrum via the qubit-coupler dispersive shift, by driving the coupler with the XY control line of Q_1 followed by a population measurement of Q_2 . The coupling between each qubit and the coupler causes a dispersive frequency shift when they are far detuned as:

$$\chi_{ic} = \frac{(g_{ic})^2(\eta_i + \eta_c)}{2(\Delta_{ic} - \eta_c)(\Delta_{ic} + \eta_i)}. \quad (D1)$$

The experimental results of coupler spectrum are shown in Fig. 8.

The qubit-coupler dispersive shift may also decrease the single-qubit gate fidelity when the coupler has a large thermal population. However, in our experiments, the single-qubit gate is implemented when the frequency detuning is large between the qubits and the coupler. Thus, the coupler's thermal population would have little effect on the single-qubit gate fidelity and overall system preparation. In addition, we believe,

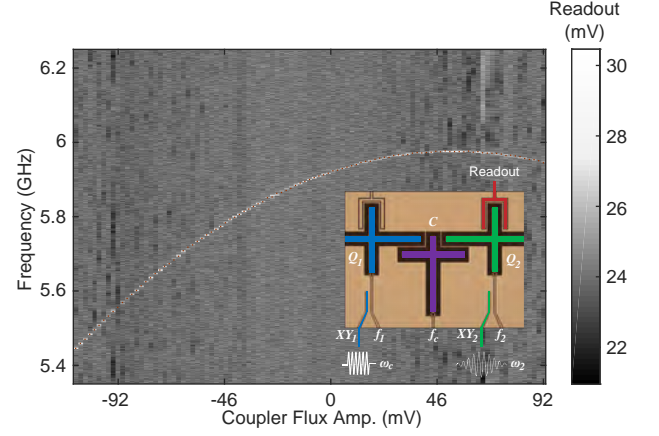


FIG. 8: Measured coupler spectrum. We drive the coupler through the XY control line of Q_1 by applying a microwave pulse at variable frequency with a rectangular envelope of a duration of 500 ns, followed by a population measurement of Q_2 with a wide selective Gaussian pulse. Inset: schematic of the measurement. The two computational qubits (Q_1 and Q_2) are shown in blue and green respectively, and the coupler is shown in purple.

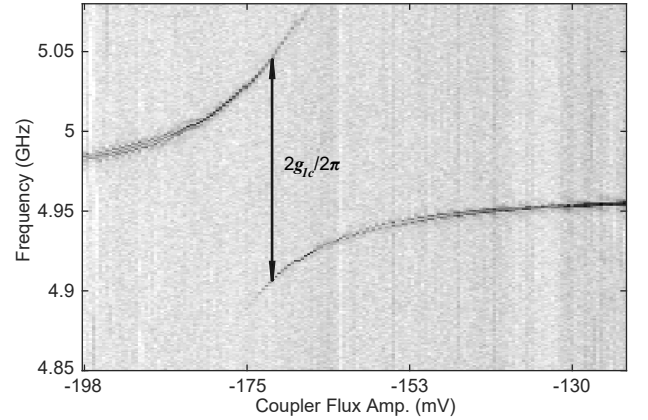


FIG. 9: Qubit-coupler anti-crossing. At the resonance point, anti-crossing of the energy level is observed and the separation characterizes the coupling strength.

through carefully designing our sample and fridge environment, the coupler thermal population can be suppressed to a very low level.

The coupling strength between each qubit and the coupler can be measured in a swap operation between them. We perform the qubit spectroscopy measurement while varying the coupler frequency and biasing the other qubit far away. The anti-crossing in the spectrum can be seen as shown in Fig. 9 and the qubit-coupler coupling strength g_{1c} can be extracted.

2. Operation range with negative coupling strength

To perform the iSWAP and \sqrt{i} SWAP gates, we need to choose an appropriate coupling strength by varying the cou-

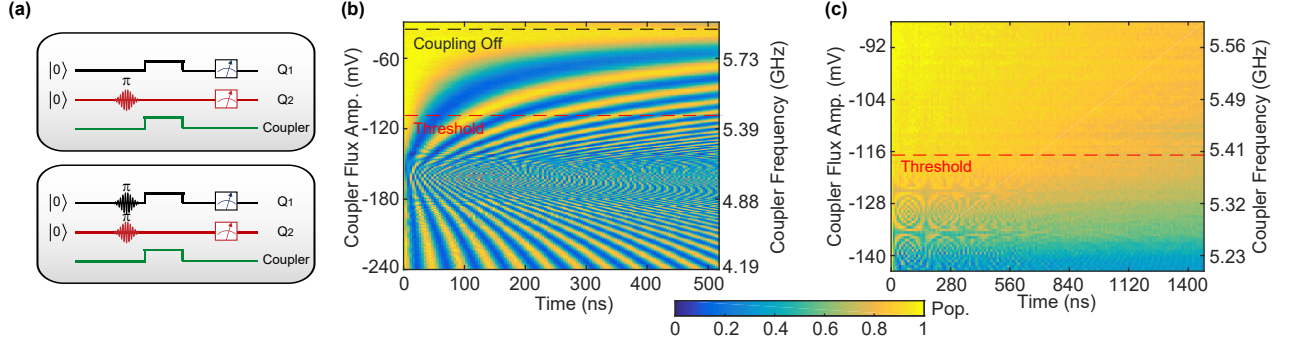


FIG. 10: Lower threshold for the coupler frequency. (a) The pulse sequences to measure the operation range with negative coupling strength. (b) A zoomed-in part of Fig. 2(b) in the main text. The swap interaction is completely turned off at the marked dark dashed line, while the red dashed line indicates the approximate threshold for non-negligible excitation of the coupler. (c) Direct leakage experiment for finding the approximate threshold of the coupler frequency. The two qubits are initialized in $|11\rangle$, then are tuned into resonance while varying the coupler frequency, and finally the population of $|11\rangle$ state is measured. The red dashed line shows the threshold of having leakage out of the computational space.

pler frequency when the two qubits are tuned into resonance. To tune the qubit and the coupler, we use fast rectangular flux pulses for the measurements shown in Fig. 3 in the main text.

In order to achieve fast two-qubit gate operations, the coupling strength needs to be large. The positive coupling strength is defined and limited by the geometry of the device, while the negative value can be varied by tuning the coupler frequency. However, the coupler frequency cannot be tuned too close to the qubit frequency for a large negative coupling strength without causing direct energy exchange between the qubit and the coupler, i.e. the leakage out of the computational space. Figure 10(b) is a zoom-in and finer sweep of Fig. 2(b) of the main text. The red dashed line shows an approximate threshold, a lower threshold for the coupler frequency, below which small ripples in the population oscillation of Q_2 start to show up, indicating non-negligible excitation of the coupler. The leakage out of the computational space can also be directly measured by monitoring the population of $|11\rangle$ state when both qubits are excited. The experimental results are shown in Fig. 10(c). Again, below the threshold of the coupler frequency, the population of $|11\rangle$ state starts to deviate from the desired exponential decay. The experimental sequences for the measurements performed in Figs. 10(b) and 10(c) are shown in Fig. 10(a).

3. Qubit coherence

One of the advantages of this prototype of coupler is the flexibility and compatibility to a large-scale architecture. The positive coupling strength is defined by the direct coupling between the two Xmon qubits, while the negative coupling is provided by the coupler. The competition between the positive direct and negative indirect coupling allows for a continuous tunability and for switching off the coupling completely. The change of sign of the coupling strength could also provide a valuable degree of freedom for future quantum simulation ap-

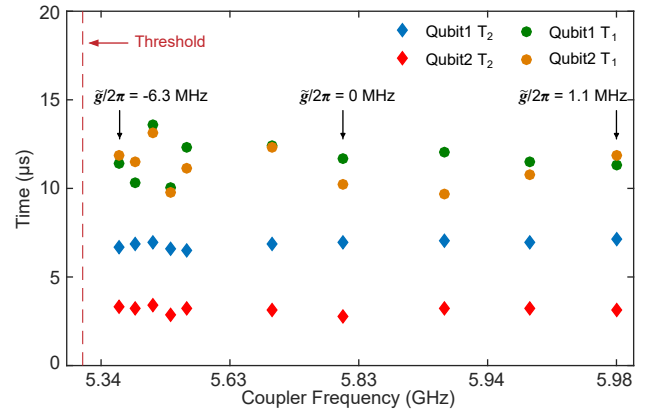


FIG. 11: Qubit coherence times vs coupler frequency. When the coupler frequency is above the threshold for non-negligible excitation of the coupler, the qubit coherence times remain nearly unaffected. Three specific coupling strengths are marked by the black arrows.

plications.

Besides, this coupler scheme can also have little impact on the qubit coherence through careful design, although the coupler is capacitively coupled to both qubits and may offer an additional decay channel to the qubits. In addition, the coupler flux bias line may inductively couple to the qubits and affect their coherence. We measure the qubit coherence times at different coupler frequencies, as shown in Fig. 11. In the operation range above the threshold, the qubit coherence times remain unaffected regardless of the coupling strength.

4. Calibration of the CZ gate

We first show the calibration of the standard CZ gate implemented by using rectangular flux pulses. We conduct the Ramsey measurements to extract the single qubit phase

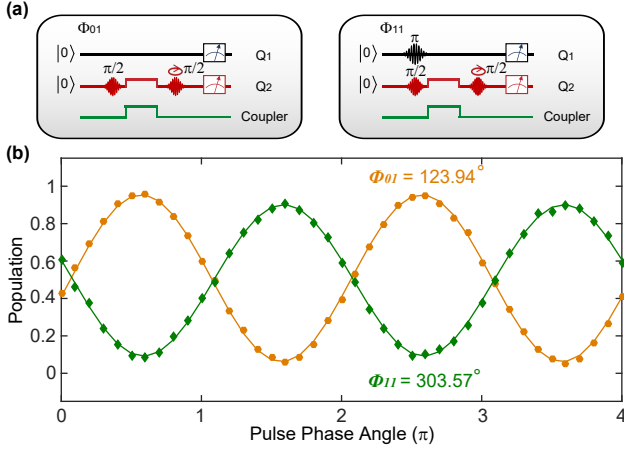


FIG. 12: The CZ gate calibration. (a) The experimental sequences to measure ϕ_{10} , phase accumulation of $|01\rangle$ with respect to $|00\rangle$, and ϕ_{11} , phase accumulation of $|11\rangle$ with respect to $|10\rangle$. (b) The probabilities of measuring $|01\rangle$ and $|11\rangle$ vs the phase of the second $\pi/2$ pulse. The sinusoidal oscillations reveal the phases acquired in the Ramsey measurements for the two-qubit states $|01\rangle \rightarrow e^{i\phi_{01}}|01\rangle$ and $|11\rangle \rightarrow e^{i\phi_{11}}|11\rangle$, respectively. The solid lines are fits to sinusoidal oscillations. With a standard CZ gate time of $t_R=222$ ns, a π phase shift between the orange and green curves is observed.

ϕ_{01} and the two-qubit conditional phase ϕ_{11} , as shown in Fig. 12(b). The solid lines are fits to sinusoidal oscillations. A π phase shift between ϕ_{01} and ϕ_{11} curves is observed when both qubits are excited. We correct the single-qubit phases in software to acquire the desired CZ gate with the unitary matrix as $\text{diag}\{1, 1, 1, -1\}$. The CZ gate fidelity is estimated to be 95.5% on average from the QPT measurement. We use the same method to calibrate the conditional π phase of the CZ gate with the dynamically decoupled regime (DDR) mentioned in the main text.

Appendix E: Simulation of the CZ gate

We simulate the CZ gates with QuTip in Python [61, 62]. First, we confirm the coupler decoherence has little effect on the CZ gates. The coupler frequency can be tuned in a large range. If the coupler frequency is far detuned from its sweet spot, the dephasing of the coupler will increase significantly. We compare the CZ gate fidelities for two cases in which the coupler dephasing time $T_2 = 5 \mu\text{s}$ and $T_2 = 0.5 \mu\text{s}$, and find there is nearly no difference between them. This is because the coupler remains almost on the ground state for the whole process.

We then simulate the standard CZ gate implemented by the rectangular flux pulse (with ‘mesolve’ in QuTip). The population evolution of each state with an initial state $|Q_1 C Q_2\rangle = | + 0 + \rangle$ is shown in Fig. 13(a), where $|+\rangle = (|g\rangle + |e\rangle)/\sqrt{2}$. In this case, the coupler frequency is tuned to 5.337 GHz and the total qubit-qubit coupling is negative. We observe significant high-frequency oscillation between $|101\rangle$ and $|200\rangle$.

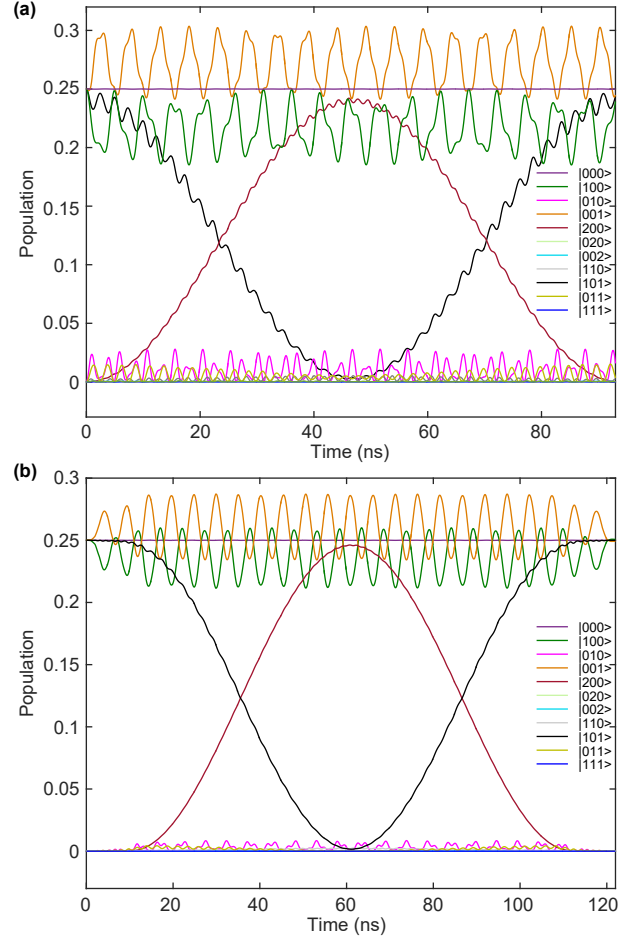


FIG. 13: Simulation of the population evolution of each state during the CZ gate with an initial joint qubit-coupler state $|Q_1 C Q_2\rangle = | + 0 + \rangle$. (a) CZ gate with rectangular flux pulses. (b) CZ gate with DDR.

This non-ideality comes from the population exchange between the coupler and the qubit, evidenced by the oscillation between $|010\rangle$ and $|100\rangle$. The swap oscillation between $|001\rangle$ and $|100\rangle$ is owing to the anharmonicity of the qubits. After a synchronization optimization strategy [60], we can achieve the fidelity of this type of CZ gate $F = 98.75\%$ in 90 ns with no system coherence.

As a comparison, the population evolution of each state for the CZ gate with the DDR scheme with the same initial state $|Q_1 C Q_2\rangle = | + 0 + \rangle$ and with the same solving methods is shown in Fig. 13(b). In this simulation, the gate time is 120 ns including DDR. The oscillation amplitude between the coupler and Q_1 decreases significantly when the coupler is turned on. If we use a slower cosine rising edge, the oscillation amplitude gets even smaller, but at the cost of a longer operation time. Most importantly, when we slowly turn off the coupler by tuning up the coupler frequency, the swap oscillation between the coupler and Q_1 gets much weaker, so the population of the coupler would slowly oscillate back into the computational space.

Based on simulation, this CZ gate fidelity could be as high as $F = 99.998\%$ after careful synchronization optimization strategy [60], provided there is no system decoherence. Given the experimental coherence times, a simulated CZ gate fidelity $F = 98.1\%$ is acquired, in good agreement with the measured $F = 98.3 \pm 0.6\%$ in the main text. In fact, such variations of the experimental gate fidelity are mainly due to two reasons. First, in our experiment, the measured histogram threshold between the ground state and the excited state of each qubit could fluctuate with time due to low frequency drift in the measurement setup. Following the Bayes rule calibration method (details can be found in Appendix C), we would acquire a measurement fluctuation distribution, and thus a variation of the gate fidelity. Second, the coherence of each qubit also varies with time. On one hand, this can affect the gate performance and thus lead to a fluctuating CZ gate fidelity; on the other hand, the simulated gate fidelity sensitively depends on the coherence times we use. Our simulation shows that the CZ gate fidelity can be improved from $F = 98.1\%$ to $F = 98.3\%$ by increasing T_2 of each qubit by only about 10%.

In addition, we also follow the method developed in Ref. 55 to extract error sources in our experimental CZ gate. We find that the decoherence error is the main error source with a contribution of about 1.14%. Other errors, contributing only 0.56% in total, may come from the state preparation and measurement errors (details can be found in Appendix B).

Because of the unwanted transitions, we could not acquire a complete geometric π phase for the CZ gate with DDR. The simulation shows the geometric contribution to the π phase is about 98.3%. We have to tune the operation point slightly away from the resonance between $|101\rangle$ and $|200\rangle$ to accumulate a small dynamical phase (about 3 degrees) to realize the required π phase.

With the extra degree of freedom provided by the tunable coupler, a more efficient pulse shape could be optimized to achieve a CZ gate with a higher fidelity and lower unwanted leakage in future experiments. This deserves future exploration.

* These two authors contributed equally to this work.

† Electronic address: ypsong@mail.tsinghua.edu.cn

‡ Electronic address: lmduan@tsinghua.edu.cn

§ Electronic address: luyansun@tsinghua.edu.cn

- [1] J. S. Otterbach, R. Manenti, N. Alidoust, A. Bestwick, M. Block, B. Bloom, S. Caldwell, N. Didier, E. S. Fried, S. Hong, *et al.*, “Unsupervised machine learning on a hybrid quantum computer,” [arXiv:1712.05771](https://arxiv.org/abs/1712.05771) (2017).
- [2] A. Kandala, A. Mezzacapo, K. Temme, M. Takita, M. Brink, J. M. Chow, and J. M. Gambetta, “Hardware-efficient variational quantum eigensolver for small molecules and quantum magnets,” *Nature* **549**, 242 (2017).
- [3] F. Arute, K. Arys, R. Babbush, D. Bacon, J. C. Bardin, R. Barends, R. Biswas, S. Boixo, F. G. S. L. Brandao, D. A. Buell, *et al.*, “Quantum supremacy using a programmable superconducting processor,” *Nature* **574**, 505 (2019).
- [4] C. Song, K. Xu, H. Li, Y.-R. Zhang, X. Zhang, W. Liu, Q. Guo, Z. Wang, W. Ren, J. Hao, *et al.*, “Generation of multicomponent atomic schrödinger cat states of up to 20 qubits,” *Science* **365**, 574 (2019).
- [5] Z. Yan, Y. Zhang, M. Gong, Y. Wu, Y. Zheng, S. Li, C. Wang, F. Liang, J. Lin, Y. Xu, *et al.*, “Strongly correlated quantum walks with a 12-qubit superconducting processor,” *Science* **364**, 753 (2019).
- [6] R. Ma, B. Saxberg, C. Owens, N. Leung, Y. Lu, J. Simon, and D. I. Schuster, “A dissipatively stabilized mott insulator of photons,” *Nature* **566**, 51 (2019).
- [7] A. J. Kollár, M. Fitzpatrick, and A. A. Houck, “Hyperbolic lattices in circuit quantum electrodynamics,” *Nature* **571**, 45 (2019).
- [8] C. K. Andersen, A. Remm, S. Lazar, S. Krinner, N. Lacroix, G. J. Norris, M. Gabureac, C. Eichler, and A. Wallraff, “Repeated quantum error detection in a surface code,” [arXiv:1912.09410](https://arxiv.org/abs/1912.09410) (2019).
- [9] I. Buluta and F. Nori, “Quantum simulators,” *Science* **326**, 108 (2009).
- [10] A. A. Houck, H. E. Türeci, and J. Koch, “On-chip quantum simulation with superconducting circuits,” *Nat. Phys.* **8**, 292 (2012).
- [11] I. M. Georgescu, S. Ashhab, and F. Nori, “Quantum simulation,” *Rev. Mod. Phys.* **86**, 153 (2014).
- [12] M. H. Devoret and R. J. Schoelkopf, “Superconducting circuits for quantum information: an outlook,” *Science* **339**, 1169 (2013).
- [13] E. T. Campbell, B. M. Terhal, and C. Vuillot, “Roads towards fault-tolerant universal quantum computation,” *Nature* **549**, 172 (2017).
- [14] J. Majer, J. M. Chow, J. M. Gambetta, J. Koch, B. R. Johnson, J. A. Schreier, L. Frunzio, D. I. Schuster, A. A. Houck, A. Wallraff, *et al.*, “Coupling superconducting qubits via a cavity bus,” *Nature* **449**, 443 (2007).
- [15] L. DiCarlo, J. M. Chow, J. M. Gambetta, L. S. Bishop, B. R. Johnson, D. I. Schuster, J. Majer, A. Blais, L. Frunzio, S. M. Girvin, *et al.*, “Demonstration of two-qubit algorithms with a superconducting quantum processor,” *Nature* **460**, 240 (2009).
- [16] J. Kelly, R. Barends, A. G. Fowler, A. Megrant, E. Jeffrey, T. C. White, D. Sank, J. Y. Mutus, B. Campbell, Y. Chen, *et al.*, “State preservation by repetitive error detection in a superconducting quantum circuit,” *Nature* **519**, 66 (2015).
- [17] J. M. Chow, A. D. Córcoles, J. M. Gambetta, C. Rigetti, B. R. Johnson, J. A. Smolin, J. R. Rozen, G. A. Keefe, M. B. Rothwell, M. B. Ketchen, *et al.*, “Simple all-microwave entangling gate for fixed-frequency superconducting qubits,” *Phys. Rev. Lett.* **107**, 080502 (2011).
- [18] S. Sheldon, E. Magesan, J. M. Chow, and J. M. Gambetta, “Procedure for systematically tuning up cross-talk in the cross-resonance gate,” *Phys. Rev. A* **93**, 060302 (2016).
- [19] L. Zhou, S. Yang, Y.-x. Liu, C. P. Sun, and F. Nori, “Quantum zeno switch for single-photon coherent transport,” *Phys. Rev. A* **80**, 062109 (2009).
- [20] J. D. Strand, M. Ware, F. Beaudoin, T. A. Ohki, B. R. Johnson, A. Blais, and B. L. T. Plourde, “First-order sideband transitions with flux-driven asymmetric transmon qubits,” *Phys. Rev. B* **87**, 220505 (2013).
- [21] Y. X. Liu, C. X. Wang, H. C. Sun, and X. B. Wang, “Coexistence of single- and multi-photon processes due to longitudinal couplings between superconducting flux qubits and external fields,” *New J. Phys.* **16**, 015031 (2014).
- [22] Z.-Y. Xue, J. Zhou, and Z. D. Wang, “Universal holonomic quantum gates in decoherence-free subspace on superconduct-

- ing circuits,” *Phys. Rev. A* **92**, 022320 (2015).
- [23] Y. Wu, L. Yang, Y. Zheng, H. Deng, Z. Yan, Y. Zhao, K. Huang, W. J. Munro, K. Nemoto, D. Zheng, *et al.*, “An efficient and compact quantum switch for quantum circuits,” *npj Quantum Information* **4**, 50 (2018).
- [24] S. A. Caldwell, N. Didier, C. A. Ryan, E. A. Sete, A. Hudson, P. Karalekas, R. Manenti, M. P. da Silva, R. Sinclair, E. Acala, *et al.*, “Parametrically activated entangling gates using transmon qubits,” *Phys. Rev. Applied* **10**, 034050 (2018).
- [25] M. Reagor, C. B. Osborn, N. Tezak, A. Staley, G. Prawiroatmodjo, M. Scheer, N. Alidoust, E. A. Sete, N. Didier, M. P. da Silva, *et al.*, “Demonstration of universal parametric entangling gates on a multi-qubit lattice,” *Sci. Adv.* **4**, eaao3603 (2018).
- [26] X. Li, Y. Ma, J. Han, T. Chen, Y. Xu, W. Cai, H. Wang, Y. Song, Z.-Y. Xue, Z.-q. Yin, *et al.*, “Perfect quantum state transfer in a superconducting qubit chain with parametrically tunable couplings,” *Phys. Rev. Applied* **10**, 054009 (2018).
- [27] T. Chen and Z.-Y. Xue, “Nonadiabatic geometric quantum computation with parametrically tunable coupling,” *Phys. Rev. Applied* **10**, 054051 (2018).
- [28] W. Cai, J. Han, F. Mei, Y. Xu, Y. Ma, X. Li, H. Wang, Y. P. Song, Z.-Y. Xue, Z.-q. Yin, *et al.*, “Observation of topological magnon insulator states in a superconducting circuit,” *Phys. Rev. Lett.* **123**, 080501 (2019).
- [29] Y. Xu, Z. Hua, T. Chen, X. Pan, X. Li, J. Han, W. Cai, Y. Ma, H. Wang, Y. P. Song, *et al.*, “Experimental implementation of universal nonadiabatic geometric quantum gates in a superconducting circuit,” *Phys. Rev. Lett.* **124**, 230503 (2020).
- [30] Y.-X. Liu, L. F. Wei, J. S. Tsai, and F. Nori, “Controllable coupling between flux qubits,” *Phys. Rev. Lett.* **96**, 067003 (2006).
- [31] A. Niskanen, K. Harrabi, F. Yoshihara, Y. Nakamura, S. Lloyd, and J. Tsai, “Quantum coherent tunable coupling of superconducting qubits,” *Science* **316**, 723 (2007).
- [32] S. H. W. van der Ploeg, A. Izmalkov, A. M. van den Brink, U. Hübner, M. Grajcar, E. Il’ichev, H.-G. Meyer, and A. M. Zagorskin, “Controllable coupling of superconducting flux qubits,” *Phys. Rev. Lett.* **98**, 057004 (2007).
- [33] R. Harris, A. J. Berkley, M. W. Johnson, P. Bunyk, S. Govorkov, M. C. Thom, S. Uchaikin, A. B. Wilson, J. Chung, E. Holtham, *et al.*, “Sign- and magnitude-tunable coupler for superconducting flux qubits,” *Phys. Rev. Lett.* **98**, 177001 (2007).
- [34] M. S. Allman, F. Altomare, J. D. Whittaker, K. Cicak, D. Li, A. Sirois, J. Strong, J. D. Teufel, and R. W. Simmonds, “rf-squid-mediated coherent tunable coupling between a superconducting phase qubit and a lumped-element resonator,” *Phys. Rev. Lett.* **104**, 177004 (2010).
- [35] R. Bialczak, M. Ansmann, M. Hofheinz, M. Lenander, E. Lucero, M. Neeley, A. O. Connell, D. Sank, H. Wang, M. Weides, *et al.*, “Fast tunable coupler for superconducting qubits,” *Phys. Rev. Lett.* **106**, 060501 (2011).
- [36] Y. Chen, C. Neill, P. Roushan, N. Leung, M. Fang, R. Barends, J. Kelly, B. Campbell, Z. Chen, B. Chiaro, *et al.*, “Qubit architecture with high coherence and fast tunable coupling,” *Phys. Rev. Lett.* **113**, 220502 (2014).
- [37] D. C. McKay, S. Filipp, A. Mezzacapo, E. Magesan, J. M. Chow, and J. M. Gambetta, “Universal gate for fixed-frequency qubits via a tunable bus,” *Phys. Rev. Applied* **6**, 064007 (2016).
- [38] Y. Lu, S. Chakram, N. Leung, N. Earnest, R. K. Naik, Z. Huang, P. Groszkowski, E. Kapit, J. Koch, and D. I. Schuster, “Universal stabilization of a parametrically coupled qubit,” *Phys. Rev. Lett.* **119**, 150502 (2017).
- [39] M. Kounalakis, C. Dickel, J. M., C. Dickel, C. Dickel, N. K. Langford, and G. A. Steele, “Tuneable hopping and nonlinear cross-kerr interactions in a high-coherence superconducting circuit,” *npj Quantum Information* **38**, 1 (2018).
- [40] Q.-M. Chen, Y.-x. Liu, L. Sun, and R.-B. Wu, “Tuning the coupling between superconducting resonators with collective qubits,” *Phys. Rev. A* **98**, 042328 (2018).
- [41] C. Neill, P. Roushan, K. Kechedzhi, S. Boixo, S. Isakov, V. Smelyanskiy, A. Megrant, B. Chiaro, A. Dunsworth, K. Arya, *et al.*, “A blueprint for demonstrating quantum supremacy with superconducting qubits,” *Science* **360**, 195 (2018).
- [42] P. Mundada, G. Zhang, T. Hazard, and A. Houck, “Suppression of qubit crosstalk in a tunable coupling superconducting circuit,” *Phys. Rev. Applied* **12**, 054023 (2019).
- [43] F. Yan, P. Krantz, Y. Sung, M. Kjaergaard, D. L. Campbell, T. P. Orlando, S. Gustavsson, and W. D. Oliver, “Tunable coupling scheme for implementing high-fidelity two-qubit gates,” *Phys. Rev. Applied* **10**, 054062 (2018).
- [44] J. Q. You and F. Nori, “Atomic physics and quantum optics using superconducting circuits,” *Nature* **474**, 589 (2011).
- [45] X. Gu, A. F. Kockum, A. Miranowicz, Y. xi Liu, and F. Nori, “Microwave photonics with superconducting quantum circuits,” *Physics Reports* **718-719**, 1 (2017).
- [46] P. Krantz, M. Kjaergaard, F. Yan, T. P. Orlando, S. Gustavsson, and W. D. Oliver, “A quantum engineer’s guide to superconducting qubits,” *Appl. Phys. Rev.* **6**, 021318 (2019).
- [47] J. M. Martinis and M. R. Geller, “Fast adiabatic qubit gates using only σ_z control,” *Phys. Rev. A* **90**, 022307 (2014).
- [48] S.-L. Zhu and P. Zanardi, “Geometric quantum gates that are robust against stochastic control errors,” *Phys. Rev. A* **72**, 020301 (2005).
- [49] R. Barends, J. Kelly, A. Megrant, D. Sank, E. Jeffrey, Y. Chen, Y. Yin, B. Chiaro, J. Mutus, C. Neill, *et al.*, “Coherent Josephson qubit suitable for scalable quantum integrated circuits,” *Phys. Rev. Lett.* **111**, 080502 (2013).
- [50] R. Barends, J. Kelly, A. Megrant, A. Veitia, D. Sank, E. Jeffrey, T. C. White, J. Mutus, A. G. Fowler, B. Campbell, *et al.*, “Superconducting quantum circuits at the surface code threshold for fault tolerance,” *Nature* **508**, 500 (2014).
- [51] A. Blais, J. Gambetta, A. Wallraff, D. I. Schuster, S. M. Girvin, M. H. Devoret, and R. J. Schoelkopf, “Quantum-information processing with circuit quantum electrodynamics,” *Phys. Rev. A* **75**, 032329 (2007).
- [52] S. Bravyi, D. P. DiVincenzo, and D. Loss, “Schrieffer–Wolff transformation for quantum many-body systems,” *Annals of physics* **326**, 2793 (2011).
- [53] M. Reed, *Entanglement and quantum error correction with superconducting qubits* (Yale University, 2013).
- [54] J. M. Chow, *Quantum information processing with superconducting qubits* (Yale University, 2010).
- [55] A. N. Korotkov, “Error matrices in quantum process tomography,” *arXiv:1309.6405* (2013).
- [56] F. W. Strauch, P. R. Johnson, A. J. Dragt, C. J. Lobb, J. R. Anderson, and F. C. Wellstood, “Quantum logic gates for coupled superconducting phase qubits,” *Phys. Rev. Lett.* **91**, 167005 (2003).
- [57] M. D. Reed, L. DiCarlo, S. E. Nigg, L. Sun, L. Frunzio, S. M. Girvin, and R. J. Schoelkopf, “Realization of three-qubit quantum error correction with superconducting circuits,” *Nature* **482**, 382 (2012).
- [58] S. Li, A. D. Castellano, S. Wang, Y. Wu, M. Gong, Z. Yan, H. Rong, H. Deng, C. Zha, C. Guo, *et al.*, “Realisation of high-fidelity nonadiabatic CZ gates with superconducting qubits,” *npj Quantum Information* **5**, 84 (2013).
- [59] L. Viola and S. Lloyd, “Dynamical suppression of decoherence

- in two-state quantum systems,” *Phys. Rev. A* **58**, 2733 (1998).
- [60] R. Barends, C. Quintana, A. Petukhov, Y. Chen, D. Kafri, K. Kechedzhi, R. Collins, O. Naaman, S. Boixo, F. Arute, *et al.*, “Diabatic gates for frequency-tunable superconducting qubits,” *Phys. Rev. Lett.* **123**, 210501 (2019).
- [61] J. R. Johansson, P. D. Nation, and F. Nori, “Qutip: An open-source python framework for the dynamics of open quantum systems,” *Comp. Phys. Comm.* **183**, 1760 (2012).
- [62] J. R. Johansson, P. D. Nation, and F. Nori, “Qutip 2: A python framework for the dynamics of open quantum systems,” *Comp. Phys. Comm.* **184**, 1234 (2013).
- [63] A. Dunsworth, R. Barends, Y. Chen, Z. Chen, B. Chiaro, A. Fowler, B. Foxen, E. Jeffrey, J. Kelly, P. Klimov, *et al.*, “A method for building low loss multi-layer wiring for superconducting microwave devices,” *Appl. Phys. Lett.* **112**, 063502 (2018).
- [64] J. Kelly, R. Barends, B. Campbell, Y. Chen, Z. Chen, B. Chiaro, A. Dunsworth, A. G. Fowler, I.-C. Hoi, E. Jeffrey, *et al.*, “Optimal quantum control using randomized benchmarking,” *Phys. Rev. Lett.* **112**, 240504 (2014).
- [65] O. Kyriienko and A. S. Sørensen, “Floquet quantum simulation with superconducting qubits,” *Phys. Rev. Applied* **9**, 064029 (2018).
- [66] G. Zhu, D. G. Ferguson, V. E. Manucharyan, and J. Koch, “Circuit qed with fluxonium qubits: Theory of the dispersive regime,” *Phys. Rev. B* **87**, 024510 (2013).
- [67] R. Krishnan and J. A. Pople, “Approximate fourth-order perturbation theory of the electron correlation energy,” *International Journal of Quantum Chemistry* **14**, 91 (1978).
- [68] M. A. Nielsen and I. Chuang, “Quantum computation and quantum information,” (2002).
- [69] Z. Chen, A. Megrant, J. Kelly, R. Barends, J. Bochmann, Y. Chen, B. Chiaro, A. Dunsworth, E. Jeffrey, J. Mutus, *et al.*, “Fabrication and characterization of aluminum airbridges for superconducting microwave circuits,” *Appl. Phys. Lett.* **104**, 052602 (2014).
- [70] B. Chiaro, A. Megrant, A. Dunsworth, Z. Chen, R. Barends, B. Campbell, Y. Chen, A. Fowler, I. C. Hoi, E. Jeffrey, *et al.*, “Dielectric surface loss in superconducting resonators with flux-trapping holes,” *Superconductor Science and Technology* **29**, 104006 (2016).
- [71] M. Hatridge, R. Vijay, D. H. Slichter, J. Clarke, and I. Siddiqi, “Dispersive magnetometry with a quantum limited SQUID parametric amplifier,” *Phys. Rev. B* **83**, 134501 (2011).
- [72] S. S. Roy, A. Shukla, and T. S. Mahesh, “NMR implementation of a quantum delayed-choice experiment,” *Phys. Rev. A* **85**, 022109 (2012).
- [73] A. Kamal, A. Marblestone, and M. H. Devoret, “Signal-to-pump back action and self-oscillation in double-pump Josephson parametric amplifier,” *Phys. Rev. B* **79**, 184301 (2009).
- [74] K. W. Murch, S. J. Weber, C. Macklin, and I. Siddiqi, “Observing single quantum trajectories of a superconducting quantum bit,” *Nature* **502**, 211 (2013).
- [75] F. Motzoi, J. M. Gambetta, P. Rebentrost, and F. K. Wilhelm, “Simple pulses for elimination of leakage in weakly nonlinear qubits,” *Phys. Rev. Lett.* **103**, 110501 (2009).